Hyperfine structure and collisions in three-photon Rydberg electromagnetically induced transparency

Alisher Duspayev ●[*,†] and Georg Raithel ●

Department of Physics, University of Michigan, Ann Arbor, Michigan 48109, USA

Multiphoton electromagnetically induced transparency (EIT) of atomic vapors involves several intermediate atomic levels. The substructure of these levels and their collisional interactions can drastically alter experimental EIT signals. Here we report on hyperfine structure and collision effects in three-photon Rydberg EIT on the cascade $5S_{1/2} \rightarrow 5P_{1/2} \rightarrow 5D_{3/2} \rightarrow 25F_{5/2}$ in a room-temperature ^{85}Rb vapor cell. In our measurements of EIT spectra, we identify two types of EIT signatures that correspond with distinct excitation pathways and atomic velocity classes in the atomic vapor. The $5D_{3/2}$ hyperfine structure and Autler-Townes splittings lead to complex patterns in the EIT spectra, which we analyze with the aid of 10-level EIT simulations. Adding 50 mTorr of Ar gas alters the EIT spectra and induces an additional, third EIT mode. Based on our simulation results, we attribute these changes to hyperfine collisions in the Rb $5D_{3/2}$ level. Our study may become useful in quantum technologies involving Rydberg EIT and hyperfine collisions in vapor cells, including noninvasive spatiotemporally resolved electric-field sensing of electric fields in low-pressure plasmas.

I. INTRODUCTION

Electromagnetically induced transparency (EIT) [1] has become an important technique for modern research in quantum optics [2], quantum information processing [3], and Rydberg-atom-based field sensing [4–6]. Focusing on the latter application, EIT offers simple, yet efficient and nondestructive detection of Rydberg states in room-temperature alkali-metal-atom vapors. Although most of the groundbreaking work in these systems has been performed with two-photon schemes, there is an interest to go beyond that [7,8]. Three-photon Rydberg-EIT schemes can be realized with all-infrared lasers [9–11], which allows one to cancel Doppler shifts [12] and to excite Rydberg states with angular momentum $\ell \geqslant 3$ in warm vapors [13–15]. All-infrared EIT laser schemes also reduce photoelectric effects and resultant light-induced electric fields in cells [16]. These features could be beneficial for electric field measurements in the VHF and UHF radio bands [14,17,18] and DC electric field sensing [13,19] for applications in plasma physics and technology [20–22] as well as microfield diagnostics [23] that occur within in-vacuum focused-ion-beam sources [24–27].

A typical three-photon Rydberg-EIT cascade scheme involves a stable ground state, two rapidly decaying intermediate states, and a high-lying metastable Rydberg state. These states are coupled by three laser fields. A suitable example in rubidium atom is the cascade system $5S_{1/2} \rightarrow 5P_{J'} \rightarrow 5D_{J''} \rightarrow nF_{J'''}$ with an $\ell = 3$ Rydberg state, with principal quantum number n. The hyperfine structures of the intermediate states range from a few tens of MHz to hundreds of MHz, leading to line splittings in the EIT spectra [28,29] and interference of transition amplitudes in excitation channels [30]. Hyperfine effects lead to increased complexity in EIT spectra [29,31]. In some cases, it is possible to eliminate the hyperfine effects by using intermediate-state detunings in the EIT cascade system that are much larger than the hyperfine splittings [8,13], at the expense of reduced EIT signal strength. Conversely, hyperfine-changing collisions at small intermediate-state detunings introduce additional quantum degrees of freedom within the driven atomic vapor that may become useful [32].

Here we investigate hyperfine-induced structures in the exemplary three-photon-cascade EIT system $5S_{1/2} \rightarrow 5P_{1/2} \rightarrow 5D_{3/2} \rightarrow 25F_{5/2}$ in ^{85}Rb. We obtain EIT spectra on a two-dimensional map spanned by the detuning Δ_D of the laser driving the $5P_{1/2} \rightarrow 5D_{3/2}$ transition (dressing laser) and the detuning Δ_R of the laser driving the $5D_{3/2} \rightarrow nF_{5/2}$ Rydberg transition (coupler laser). The collected experimental Rydberg-EIT spectra exhibit a rich structure of hyperfine-induced features that we analyze with the aid of numerical models. We observe and explain several three-photon EIT modes. In the near-resonant region, $\Delta_D \approx 0$ and $|\Delta_R| \lesssim 400$ MHz, we find a set of EIT features that are generated by the hyperfine structure of the intermediate $5D_{3/2}$ level. Data taken in the presence of an additional low-pressure inert gas reveal an extra EIT branch that is attributed to hyperfine collisions of the intermediate levels of the three-photon EIT cascade. The collisional EIT branch provide insight into which types of inert-gas-induced interactions are the most relevant.

II. EXPERIMENTAL SETUP

Our experimental setup is sketched in Fig. 1(a) with the diagram of the relevant ^{85}Rb energy levels in Fig. 1(b).

---

*Contact author: alisherd@umich.edu

†Present address: Department of Physics and Joint Quantum Institute, University of Maryland, College Park, Maryland 20742, USA.
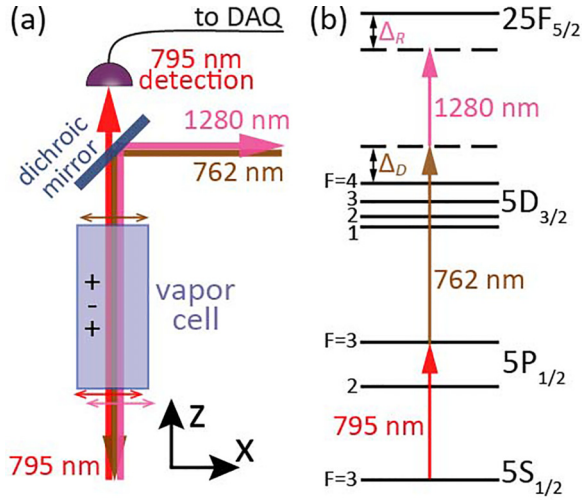
032821-1

FIG. 1. Experimental setup (a) and relevant ^{85}Rb energy-level diagram (b). All lasers are linearly polarized parallel to the x axis. The 795-nm and 1280-nm lasers propagate in the $+z$ direction, and the 762-nm laser propagates in the $-z$ direction ("+ - +" configuration). The diagram in (b) includes the hyperfine structures of the $5P_{1/2}$ and the $5D_{3/2}$ states (not to scale).

Rydberg atoms are excited in a room-temperature vapor cell using three infrared lasers. The lowest stage, which constitutes the EIT probe, has a wavelength $\lambda_P \approx 795$ nm and is frequency locked to the $|5S_{1/2}, F = 3\rangle \rightarrow |5P_{1/2}, F' = 3\rangle$ transition using saturated-absorption spectroscopy in a first reference vapor cell. The probe laser has a detuning $\Delta_P \approx 0$ from said transition and is sent to the measurement cell via a polarization-maintaining (PM) fiber. The probe light transmitted through the measurement cell is detected as shown in Fig. 1(a).

The intermediate excitation laser, which provides the EIT dressing beam, has a wavelength $\lambda_D \approx 762$ nm. The 762-nm laser is split into two beams. One passes through a fiber-coupled electro-optic modulator (EOM) and then through a second reference vapor cell. There it is overlapped with and counter-aligned to a 795-nm beam sample from the frequency-locked probe laser. The EOM has a near-linear response from DC to about 10 GHz and is driven by a tunable radio-frequency (RF) source. The 762-nm beam passing through the second reference cell has three significant components, namely, the carrier and the first-order frequency modulation (FM) sidebands, each of which generates a two-photon EIT signal in the second reference cell on the $5S_{1/2} \rightarrow 5P_{1/2} \rightarrow 5D_{3/2}$ cascade. The 762-nm laser is frequency locked to the reference EIT signal on one of the FM sidebands. The carrier is scanned by changing the frequency of the EOM drive. The second, unmodulated 762-nm beam, which has a frequency equal to that of the carrier passing through the second reference vapor cell, is sent via another PM fiber to the measurement cell. The dressing-beam detuning with respect to the $|5P_{1/2}, F' = 3\rangle \rightarrow |5D_{3/2}, F'' = 4\rangle$ hyperfine transition, denoted Δ_D [see Fig. 1(b)], is varied via the RF frequency of the EOM driver. The Δ_D scan range is about 100 MHz wide and is approximately centered to the 30-MHz wide manifold of the optically coupled ^{85}Rb $5D_{3/2}$ hyperfine states $F'' = 2$, 3, and 4.

The upper-stage laser provides the EIT coupler beam, which in the present work drives the $|5D_{3/2}, F'' = *\rangle \rightarrow |25F_{5/2}, F''' = *\rangle$ Rydberg transitions. The coupler has a wavelength $\lambda_R \approx 1280$ nm, and its detuning relative to the $|5D_{3/2}, F'' = 4\rangle \rightarrow |25F_{5/2}, F''' = *\rangle$ hyperfine component is denoted Δ_R. The allowed Rydberg hyperfine states, $F''' = 1$ to 5, are not resolved due to their minute, albeit unknown, hyperfine splittings. The detuning Δ_R is scanned by applying a linear voltage ramp to a piezoelectric tuning element in the 1280-nm laser. To linearize and calibrate the Δ_R scans, a coupler-laser beam sample is passed through an EOM that FM modulates the sample at a frequency of 125 MHz. The FM-modulated beam sample is passed through a Fabry-Pérot (FP) etalon with a free spectral range (FSR) of ≈ 375 MHz, and the transmitted sample power is measured with a photodiode. The FP etalon is air spaced, has a fixed ultra-low-expansion glass spacer, has a finesse of 70, and is housed in a temperature-stabilized fixed-pressure container. As the 1280-nm laser is scanned, the transmission of the FM-modulated 1280-nm beam sample through the FP etalon exhibits high-visibility peaks with a full width at half maximum (FWHM) of about 5 MHz and a fixed frequency spacing of 125 MHz. These are recorded simultaneously with the 795-nm EIT probe light obtained from the EIT measurement cell. There are about six FP transmission peaks in each Δ_R scan, which serve as a frequency "ruler" that allows us to map the EIT coupler scans onto a linear, calibrated Δ_R frequency axis. The FP transmission peaks also serve to correct for long-term coupler-laser frequency drifts. In this way, the frequency scans of the 1280-nm coupler laser are linearized and positioned with an accuracy and precision of ~ 1 MHz.

Most of the 1280-nm laser's power is used to seed a fiber-coupled optical amplifier to achieve sufficient coupler-beam power for Rydberg-EIT spectroscopy. To improve the signal-to-noise ratio of the EIT spectra, we use the following lock-in detection method. The 1280-nm amplifier's output beam is sent through an acousto-optic modulator (AOM). A first-order AOM diffraction mode is aligned through the measurement cell, as shown in Fig. 1(a). The AOM is used to pulse modulate the coupler beam with a 1.5 kHz square wave, which has a 50% duty cycle and which is also used as a reference for the lock-in amplifier. The detected 795-nm EIT probe signal is connected to the lock-in amplifier's input. The lock-in amplifier output presents a sensitive measure for the Rydberg-EIT that results from the presence of 1280-nm coupler light in the vapor cell. In Figs. 2(a) and 3(a), we display the lock-in amplifier's output as a function of Δ_R and Δ_D.

All three lasers are commercial external-cavity diode lasers. As depicted in Fig. 1(a), the 795-nm and the 1280-nm beams copropagate along the $+z$ direction in the measurement cell, whereas the 762-nm beam is counterpropagating to them. This configuration is referred to as $(+, -, +)$ [8]. All lasers are polarized along the x direction. The optical powers entering the measurement cell are ≈ 10 μW, ≈ 4 mW, and ≈ 10 mW, and the beams are focused down to a full width at half maximum (FWHM) of ≈ 80 μm, ≈ 250 μm, and > 250 μm for the 795-nm, 762-nm, and 1280-nm EIT beams, respectively. Using these beam parameters, we estimate the respective radial Rabi frequencies at the beam centers to be $\Omega_{PS} \approx 50$ MHz for $|5S_{1/2}, F = 3\rangle \rightarrow |5P_{1/2}, F' = 3\rangle$,
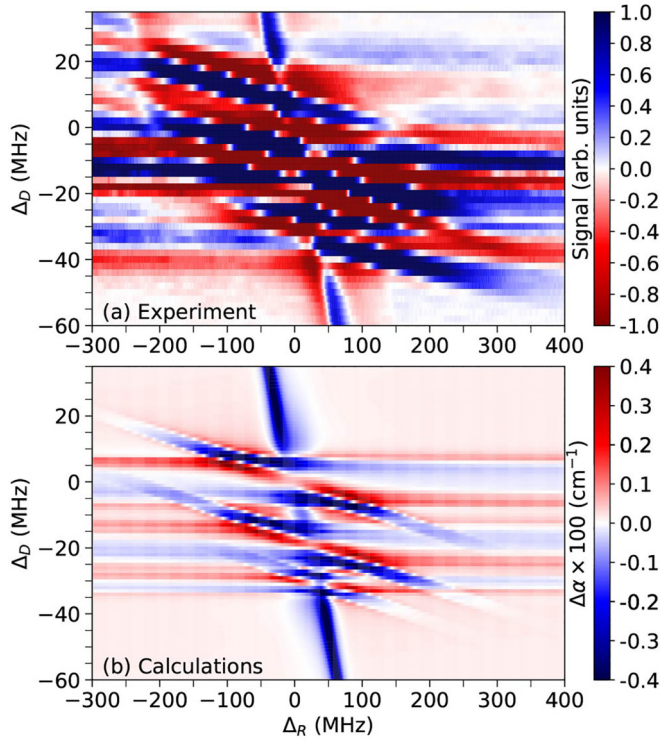
FIG. 2. (a) Map of $\bar{S}(\Delta_R, \Delta_D)$ for a Rb vapor cell free of added inert gas. Coupler- and dressing-beam detunings, Δ_R and Δ_D, are varied over respective ranges of 700 MHz and 95 MHz, with $\Delta_R = 0$, $\Delta_D = 0$ corresponding to the $|5S_{1/2}, F = 3\rangle \rightarrow |5P_{1/2}, F' = 3\rangle$ and $|5P_{1/2}, F' = 3\rangle \rightarrow |5D_{3/2}, F'' = 4\rangle$ double resonance. EIT corresponds with positive values (blue regions), and EIA with negative values (red regions). (b) Simulation results for the change of the absorption coefficient, $\Delta\alpha$, from average. Note the inverted color bar in (b), where values $\Delta\alpha > 0$ ($\Delta\alpha < 0$) correspond to EIA (EIT).

$\Omega_{DP} \approx 100$ MHz for $|5P_{1/2}, F' = 3\rangle \rightarrow |5D_{3/2}, F'' = *\rangle$, and $\Omega_{RD} \lesssim 25$ MHz for the Rydberg transitions. The $5D_{3/2}$ hyperfine splittings are several tens of MHz and are spectroscopically resolved. The unknown Rydberg $25F_{5/2}$ hyperfine structure is very small and cannot be resolved. The radial Rabi frequencies are multiplied with angular matrix elements, as described in Sec. V. All Rabi frequencies drop off from their center values according to the respective FWHM beam diameters. A dichroic mirror [see Fig. 1(a)] is used to overlap all beams and to deflect the 1280-nm light from the photodiode that detects the 795-nm EIT probe signal.

III. DATA ACQUISITION

The data are acquired in the following order. For a selected value of Δ_D, the detuning of the EIT coupler beam, Δ_R, is scanned over a range of ≈ 700 MHz with a scan duration of 100 ms. To improve the signal-to-noise ratio of the measured EIT probe signal, the coupler beam is pulse modulated at 1.5 kHz while Δ_R is being scanned, and the transmission of the EIT probe beam, T, is demodulated using the lock-in amplifier. The lock-in amplifier is referenced to the waveform that square modulates the coupler beam. The lock-in amplifier's time constant is set at 3 ms. The lock-in amplifier's phase is set once so that the magnitude of the "X" output is

largest, while the "Y" quadrature output is near zero. The "X" output constitutes the recorded signal, denoted $S_0(\Delta_R)$. It is proportional to the difference in probe transmission for the coupler laser on (T) and off (T_0),

$$S_0(\Delta_R) \approx \text{const} \times [T(\Delta_R) - T_0(\Delta_R)].$$

Positive S_0 corresponds to EIT and negative S_0 to electromagnetically induced absorption (EIA). As the coupler laser is scanned, $S_0(\Delta_R(t))$ is acquired on an oscilloscope in AC mode (time constant 50 ms). The recorded signal, $S(\Delta_R(t))$, is relative to the time average $\langle S_0(\Delta_R(t))\rangle_t$,

$$S(\Delta_R(t)) = S_0(\Delta_R(t)) - \langle S_0(\Delta_R(t))\rangle_t.$$

For each value of Δ_D, we acquire 100 to 150 scans $S(\Delta_R(t))$, which are averaged. Using the simultaneously recorded FP transmission peaks as frequency markers, the averaged time-dependent scan is converted into a function of coupler-laser detuning, Δ_R. In this way, the mild nonlinearities of the coupler-laser scan are eliminated, and the data $\bar{S}(\Delta_R)$ are rendered on a calibrated, linear Δ_R scale. The data $\bar{S}(\Delta_R)$ are then shifted by small amounts so that the Δ_R-averages are zero, i.e., $\langle \bar{S}(\Delta_R)\rangle_{\Delta_R} = 0$. The procedure is repeated for selected values of Δ_D on an equidistant grid with a step size of 2 MHz. All scans are then assembled in two-parameter maps, $\bar{S}(\Delta_R, \Delta_D)$.

IV. RESULTS WITHOUT ADDED INERT GAS

We first show results for a 7.5-cm-long Rb vapor cell that is free of additional inert gases and that is held at room temperature. Figure 2(a) shows a map of experimental EIT spectra $\bar{S}(\Delta_R, \Delta_D)$ acquired with this cell using the described method. Over a range $\Delta_D \lesssim \Omega_{DP}$, the probe absorption coefficient of the atomic vapor, α, is greatly suppressed due to two-photon EIT on the cascade $5S_{1/2} \rightarrow 5P_{1/2} \rightarrow 5D_{3/2}$, leading to high values of the probe transmission fraction, $T(\Delta_R, \Delta_D)$. The AC coupling of the scope in the above-described procedure removes the effect of two-photon EIT from the data, leaving only the three-photon EIT signal. The data $\bar{S}(\Delta_R, \Delta_D)$ are displayed on a linear color scale that ranges from -1 (red) for maximum three-photon EIA to 1 (blue) for maximum three-photon EIT.

The map exhibits several types of EIT and EIA features. First, there is a steep, singular EIT stripe that has a slope of -1 and that cuts across the map within the range $-30\,\text{MHz} \lesssim \Delta_R \lesssim 70\,\text{MHz}$. In this EIT mode, referred to as EIT mode 1, the probe laser, which has a detuning $\Delta_P \approx 0$, resonantly excites atoms that move at a velocity $v_z \approx 0$ in the probe-beam direction. The transition linewidth of 6 MHz corresponds with a velocity bandwidth $v_z \lesssim 5$ m/s of resonant atoms. The dressing and coupler lasers resonantly drive the $|5P_{1/2}, F' = 3\rangle \rightarrow |25F_{5/2}, F''' = *\rangle$ two-photon transition for atoms with $v_z \approx 0$, with intermediate detunings δ from the various $|5D_{3/2}, F'' = *\rangle$ hyperfine states. For $\Delta_D \gtrsim 20\,\text{MHz}$ or $\Delta_D \lesssim -45\,\text{MHz}$ in Fig. 2(a), the two-photon transitions $|5P_{1/2}, F' = 3\rangle \rightarrow |25F_{5/2}, F''' = *\rangle$ are relatively far-off-resonance from all $|5D_{3/2}, F'' = *\rangle$ hyperfine levels, and the respective two-photon Rabi frequencies are $\Omega_{RP} \sim \Omega_{RD}\Omega_{DP}/(2\delta)$, with one-photon Rabi frequencies of the

Rydberg and dressing transitions, Ω_{RD} and Ω_{DP}, respectively, and intermediate detunings δ depending on F''.

The two-photon couplings in EIT mode 1 undergo three intermediate-state resonances where $\delta \sim 0$ because there are three allowed intermediate $|5D_{3/2}, F''\rangle$ hyperfine states, $F'' = 4$, 3, and 2. These have respective hyperfine detunings $\delta_{HFS,F''} = 0$, -18.4 MHz, and -30.2 MHz [33]. In the EIT map, the three resonance points are at $\Delta_D = -\Delta_R = \delta_{HFS,F''}$. The resonance points, in combination with the strong dressing drive, result in a complex line pattern in the region -45 MHz $\lesssim \Delta_D \lesssim 20$ MHz. This pattern includes EIT mode 2, in which the probe and dressing transitions resonantly drive the $|5S_{1/2}, F = 3\rangle \rightarrow |5D_{3/2}, F''\rangle$ two-photon transition, while the coupler resonantly drives the $|5D_{3/2}, F''\rangle \rightarrow |25F_{5/2}, F''' = *\rangle$ one-photon transition. In our case it is $\Delta_P \approx 0$, and the EIT mode 2 is associated with atoms moving at a velocity of $v_z = -18.36 \times (\Delta_D - \delta_{HFS,F''})$ (m/s)/MHz relative to the probe-beam direction (see Sec. V). The Δ_D and Δ_R ranges over which EIT mode 2 is observed are limited by the width of the Maxwell velocity distribution of the Rb atoms in the vapor cell.

In Fig. 2(a) the EIT mode 2 gives rise to linear blue stripes with a shallow slope of $d\Delta_D/d\Delta_R \approx -0.070$. For small $\Omega_{DP} \lesssim 5$ MHz, each $|5D_{3/2}, F''\rangle$ hyperfine state would generate a single EIT mode 2 stripe intersecting the EIT mode 1 stripe at $\Delta_D = -\Delta_R = \delta_{HFS,F''}$. However, in our experiment the dressing Rabi frequencies Ω_{DP} are on the order of tens of MHz. The resultant Autler-Townes-splittings on the dressing transition tend to break the EIT mode 2 features up into two branches for each F'', leading to a total of up to six branches. As a result, near the intersection points of the steep EIT mode 1 feature (slope $d\Delta_D/d\Delta_R \approx -1$) and the shallow EIT 2 features (slope $d\Delta_D/d\Delta_R \approx -0.070$), in Fig. 2(a) we observe considerable complexity, including regions of strong EIA that break up the EIT mode 1 feature.

At certain constant values of Δ_D and large $|\Delta_R|$ Fig. 2(a) further exhibits horizontal bands of alternating EIT and EIA. These are likely caused by interference between the EIT modes 1 and 2, as well as their crosstalk with two-photon EIT on the three-level cascade $|5S_{1/2} \rightarrow |5P_{1/2}\rangle \rightarrow |5D_{3/2}\rangle$.

While some features in maps such as the one displayed in Fig. 2(a) have qualitative explanations, detailed interpretations of these features require a simulation of our three-photon EIT system. The simulations presented next will provide further insights.

V. THEORETICAL MODEL

We use a Rydberg-EIT model based on Lindblad equations [34], similar to that in [8], to determine Beer's absorption coefficient, α, for the EIT probe beam. Since all polarizations are linear and parallel, for ^{85}Rb the Hilbert space of coherently coupled states breaks up into subspaces of levels $\{|5S_{1/2}, F = 3, m_F\rangle, |5P_{1/2}, F' = 3, m_F\rangle, |5D_{3/2}, F'' = *, m_F\rangle, |25F_{5/2}, F''' = *, m_F\rangle\}$. The $F = 2$ and $F' = 2$ hyperfine states of $5S_{1/2}$ and $5P_{1/2}$, respectively, are not included because they are far-off-resonant [35]. The quantization axis is given by the polarization direction of the laser beams. Each subspace of laser-coupled states has a fixed magnetic quantum number m_F that can range from -3 to 3. The hyperfine states

of $5D_{3/2}$ are normally ordered, and the splittings between the optically coupled ones are 18.42 MHz between $F'' = 3$ and 4, and 11.81 MHz between $F'' = 2$ and 3 [33]. The hyperfine states of the Rydberg level $25F_{5/2}$ are practically degenerate, and the optically coupled ones have hyperfine quantum numbers $F''' = 1$ to 5. Therefore, the EIT simulation includes up to 10 levels, which are coupled by up to 13 allowed single-photon couplings, dependent on m_F. The Rabi frequencies for the couplings are determined as described in [36], using reduced matrix elements from [37,38]. For the radial matrix element of the Rydberg transition we use a private code. The two-photon couplings from $|5P_{1/2}, F' = 3, m_F\rangle$ to any $|25F_{5/2}, F''', m_F\rangle\}$ are generally coherent sums over multiple intermediate states $|5D_{3/2}, F'' = *, m_F\rangle$.

Subspaces for different m_F become coupled through the decay channels, leading to optical pumping. With optical pumping rates on the order of 10^7 s^{-1} and atom-field interaction times $\lesssim 1$ µs (probe beam size divided by thermal velocity), only on the order of five probe photons are scattered by each atom passing through the EIT probe region. Hence, optical pumping effects are deemed fairly weak. Therefore, in our numerical solutions of the Lindblad equation we treat the m_F manifolds separately and assume m_F-preserving decays. The simulation results for the individual m_F are averaged over the allowed m_F-range, $m_F = -3, \dots, 3$, using equal weights for the m_F. The simulations need to be conducted only for $m_F = 1$, 2, and 3 because the results depend only on $|m_F|$, and because atoms in $m_F = 0$ do not absorb π-polarized EIT probe light on the chosen $F = 3$ to $F' = 3$ EIT probe transition. Further, different atom velocities result in velocity-dependent Doppler shifts of all three laser fields, necessitating a separate numerical solution of the Lindblad equation on a sufficiently fine grid of the atom velocity in the laser beam direction, v_z. The results are velocity averaged with a weighting given by the one-dimensional Maxwell velocity distribution of the atoms in the cell [8].

The decay rates in our simulations are set as follows. The Rydberg-state decay rate is sufficiently small that it can be modeled by an effective recycling of Rydberg atoms into the $5S_{1/2}$ ground-state population. Physically, the recycling amounts to Rydberg atoms leaving and ground-state atoms entering the EIT probe region due to thermal motion in the 300-Kelvin cell. In our model, we account for the atom recycling by introducing decays from the five populated Rydberg hyperfine levels, $|25F_{5/2}, F''', m_F\rangle$ with $F''' = 1$ to 5, into $|5S_{1/2}, F = 3, m_F\rangle$ at a decay rate of $2\pi \times 0.1$ MHz. The Rb $5D_{3/2}$ lifetime has been measured to be 246 ns [39], corresponding to a decay rate of about $2\pi \times 0.7$ MHz. The $5D_{3/2}$ decay proceeds predominantly through the rapidly decaying $5P_J$ and $6P_J$ states, with $5P_{1/2}$ being the dominant intermediate state in the decay chain. In our model the $5D_{3/2}$-decay is approximated by a single decay channel from $5D_{3/2}$ to $5P_{1/2}$ with a decay rate of $2\pi \times 0.8$ MHz. The $5P_{1/2}$ to $5S_{1/2}$ decay rate is set to $2\pi \times 6$ MHz [35].

It is noted that the absence of m_F crosstalk in solving the Lindblad equation is a critical simplification because it reduces the Hilbert space dimension to only 10 states, corresponding to 100 real-valued elements of the density operator. The state space of all laser-coupled states has a dimension

of 49, and the global space of laser-coupled states plus states populated via decays is even larger, corresponding to density operators with many thousands of matrix elements (which would have to be solved for on a grid of several thousand velocities in the thermal atom sample). The Lindblad equation describing Rydberg-EIT dynamics in large Hilbert spaces can be solved using a stochastic method that utilizes ensembles of wave-function "trajectories" [40,41]. We do not believe that this approach would reveal additional insights that would become observable at the accuracy level of our present experimental study. However, in the future, the modeling of refined measurements may warrant simulations based on a quantum trajectory approach in the global Hilbert space of the system.

Figure 2(b) shows the results of a simulation performed as described above. The simulation is for radial Rabi frequencies of 24 MHz, 80 MHz, and 20 MHz for the probe, dressing, and coupler beams, respectively. All Rabi frequencies are reduced by angular factors that are mostly $\lesssim 0.5$ and that depend on all upper- and lower-state angular quantum numbers. In accordance with the experimental procedure, we display

$$\Delta\alpha(\Delta_R, \Delta_D) = \alpha(\Delta_R, \Delta_D) - \langle\alpha(\Delta_R, \Delta_D)\rangle_{\Delta_R},$$

where $\alpha(\Delta_R, \Delta_D)$ is the Beer's absorption coefficient computed on a two-dimensional grid of coupler and dressing beam detunings with a step size of 1 MHz, and the average $\langle\cdot\rangle$ is taken only over the coupler detuning, Δ_R, with Δ_D held fixed.

The computation reproduces the experimental observations quite well. We observe both EIT modes 1 and 2 discussed in Sec. IV. The computations confirm that the "fishbone" pattern of the EIT mode 2 features is due to a combination of the resolved $5D_{3/2}$ hyperfine structure and Autler-Townes splittings introduced by the dressing-beam Rabi frequencies, which are tens of MHz. Due to the small size of the probe beam relative to both the dressing and the coupler beams ($\approx 80\,\mu\text{m}$ versus $\gtrsim 250\,\mu\text{m}$), inhomogeneous broadening due to spatial variations of the dressing- and coupler-beam Rabi frequencies across the EIT probe beam's sampling volume is insignificant (as was seen in numerical modeling not presented). However, the dressing-beam Rabi frequencies depend strongly on F'' and m_F, leading to different Autler-Townes splittings for the $|5D_{3/2}, F'', m_F\rangle$ hyperfine levels. These result in six broadened branches of EIT mode 2 that intersect with the stripe for the EIT mode 1. The EIT mode 2 branches have slopes of ≈ -0.070 at Δ_R detunings far from the EIT mode 1 stripe. Finally, the pattern of horizontal, alternating EIT and EIA stripes, observed in the experimental data in Fig. 2(a) at large $|\Delta_R|$, is also qualitatively reproduced in Fig. 2(b). Deviations in the details between the experiment and the simulation are attributed, in part, to environmental magnetic fields, which are not shielded, laser polarization imperfections, and optical-pumping effects [41–44], which are neglected here.

VI. EFFECTS OF AN ADDED INERT GAS

To explore the utility of Rydberg-EIT as a diagnostic tool to measure plasma electric fields, an inert gas that is sufficiently dense to support a low-pressure plasma must be introduced. In previous work on two-photon Rydberg EIT, it was found that inert-gas collisions can reduce the visibility of EIT lines and
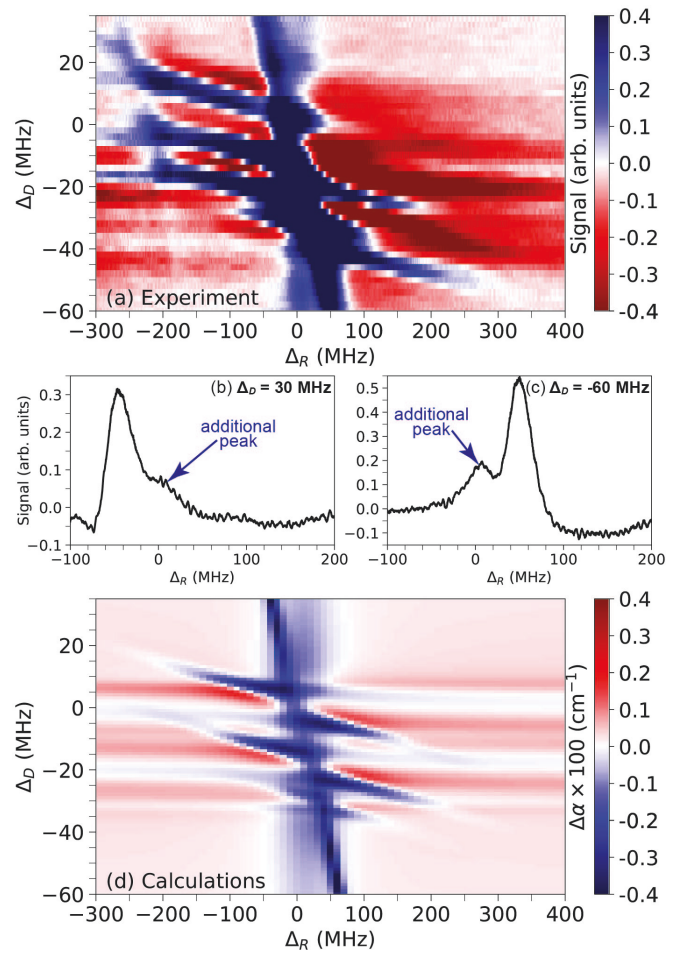

FIG. 3. (a) The same as Fig. 2(a), but for a Rb vapor cell with an added Ar gas at 50 mTorr pressure. Two individual coupler-laser scans at $\Delta_D = 30$ and -60 MHz are shown in (b) and (c), respectively. (d) The result of a simulation of $\Delta\alpha$ analogous to Fig. 2(b), but with hyperfine mixing in $5D_{3/2}$.

add additional features [45]. In the following, we investigate the effects of low-pressure argon (Ar) gas in considerably richer three-photon EIT spectra. In the experiment, we replace the 7.5-cm-long Ar-free vapor cell with a 4-cm-long cell containing a mixture of Rb vapor and 50 mTorr of Ar.

Experimental three-photon EIT spectra taken in the presence of 50 mTorr of Ar are shown in Fig. 3(a). While spectra without [Fig. 2(a)] and with 50 mTorr of Ar [Fig. 3(a)] appear qualitatively similar, there are several important differences. First, the Ar gas reduces the overall signal strength of the EIT 1 and EIT 2 modes (note the color scales are different in the figures). The EIT mode 2 features remaining in the presence of the Ar gas are most prominent in the upper-left and lower-right segments of the plot. In the intersection region between the EIT mode 1 and EIT mode 2 features, the EIT mode 1 line becomes contiguous and is not broken up by regions of strong EIA, as is the case in Fig. 2(a). The visibility of the pattern of alternating horizontal EIT and EIA stripes at large $|\Delta_R|$ and $\Delta_D \sim 0$ is reduced in Fig. 3 relative to Fig. 2. Notably, the Ar gas introduces an additional EIT feature at near-zero coupler detuning, $\Delta_R \approx 0$. This feature, which we refer to as
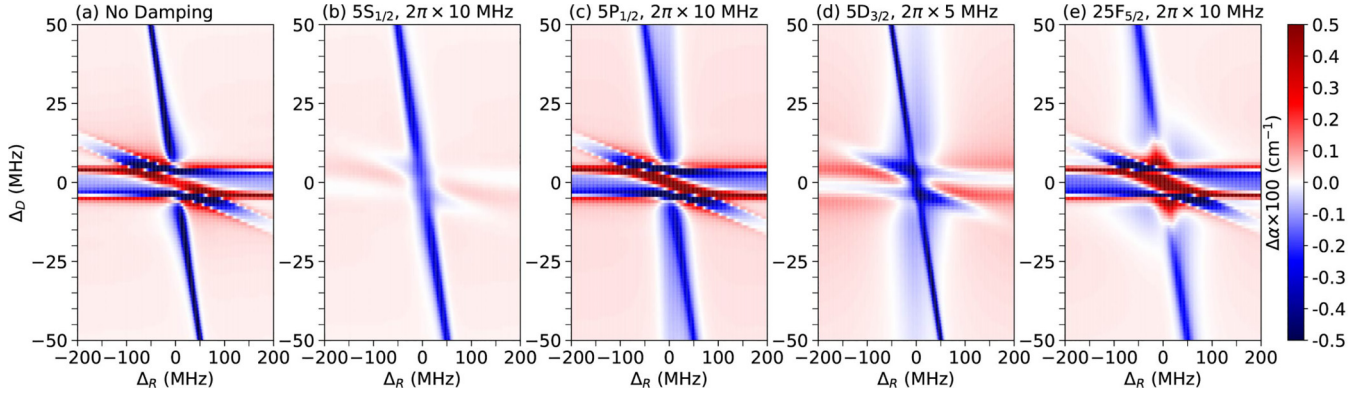
FIG. 4. Effects of collisional level dephasing of different states involved in the process of three-photon Rydberg-EIT using the cascade the $5S_{1/2} \rightarrow 5P_{1/2} \rightarrow 5D_{3/2} \rightarrow 25F_{5/2}$. In panel (a) there is no collisional level dephasing. In panels (b)–(e), collisional level dephasing is applied to the indicated states at the rates shown.

EIT mode 3, becomes visible for $\Delta_D \gtrsim 10$ MHz and $\Delta_D \lesssim -40$ MHz, and its position on the Δ_R axis is independent of Δ_D. Two instances of the EIT mode 3 in coupler-laser scans at selected values of Δ_D are shown in Figs. 3(b) and 3(c), where they are labeled as "additional peak."

It is noteworthy that the Ar gas red-shifts the Rydberg lines by ≈ -20 MHz [46,47]. Further, results qualitatively similar to those in the present work were obtained with 500 mTorr of Ar (not shown). The overall signal diminishes in strength and broadens with increasing pressure, preventing a meaningful analysis at 500 mTorr of Ar.

VII. MODELING OF INERT-GAS EFFECTS

In the following, we introduce hyperfine collisions of the Rb states in our model to obtain insight into which interactions may explain the changes between Figs. 3(a) and 2(a). For simplicity, we first use a four-level model with a single $5D_{3/2}$ and $25F_{5/2}$ state. Hyperfine-changing collisions and depolarization are modeled via a dephasing term that selectively acts upon one of the four involved states. Comparing the resultant simulated EIT maps with Fig. 3(a) then allows us to assess which type of interaction is the most consistent with the experimental data. To clarify our notation for decay rates, assume that a level $|n\rangle$ decays to level $|m\rangle$ with a population decay rate Γ_{mn}, and that level $|n\rangle$ exhibits additional dephasing (i.e., coherence decay without population decay) according to a rate γ_n. In our model, these processes would be described by damping of the form

$$\dot{\rho}_{mn} = -\frac{(\Gamma_{mn} + \gamma_n)}{2}\rho_{mn}.$$

In Figs. 4(a)–4(e) we use probe, dressing, and coupler Rabi frequencies of $2\pi \times 5$ MHz, $2\pi \times 20$ MHz, and $2\pi \times 10$ MHz, respectively, which are on the order of the magnitudes used in the experiment. We also use the above population decay rates of $2\pi \times 6$ MHz from $5P_{1/2}$ to $5S_{1/2}$, $2\pi \times 0.8$ MHz from $5D_{3/2}$ to $5P_{1/2}$, and a Rydberg-atom recycling rate of $2\pi \times 0.1$ MHz from $25F_{5/2}$ to $5S_{1/2}$. In Fig. 4(a) there is no collisional level dephasing, while in Figs. 4(b)–4(e) we add collisional dephasing at rates of $2\pi \times 10$ MHz on

$5S_{1/2}$, $2\pi \times 10$ MHz on $5P_{1/2}$, $2\pi \times 5$ MHz on $5D_{3/2}$, and $2\pi \times 10$ MHz on $25F_{5/2}$, respectively. Only one of the four levels at a time is subjected to collisional dephasing. It is seen in Figs. 4 that the four types of dephasing reduce the signal strength of the remaining EIT/EIA features by quite different degrees, allowing us to isolate potential causes for our experimental observation.

The simulation result in Fig. 4(b) eliminates $5S_{1/2}$ level dephasing as a significant cause of our experimental findings because it fails to produce the EIT mode 3, and because it almost entirely eliminates the EIT mode 2.

Next, from Fig. 4(c) we conclude that $5P_{1/2}$ level dephasing may be present at some level, because it raises the EIT mode 3 feature. However, $5P_{1/2}$ dephasing leaves the EIT mode 2 feature too strong relative to the EIT mode 1 feature. Further, the EIT mode 1 feature still remains broken up by a region of strong EIA near $\Delta_D = 0$. Moreover, $5P_{1/2}$ dephasing does not sufficiently reduce the visibility of the pattern of alternating horizontal EIT and EIA stripes at large $|\Delta_R|$.

In Fig. 4(d) we see that the $5D_{3/2}$ collisional dephasing raises the EIT mode 3 feature and attenuates both EIT modes 1 and 2 by similar amounts, while preferentially preserving the upper-left and lower-right branches of the EIT mode 2 features. Moreover, the $5D_{3/2}$ dephasing changes the EIT mode 1 into a contiguous feature that is not broken up by an EIA region near $\Delta_D = 0$. Further, the visibility of the pattern of alternating horizontal EIT and EIA stripes at large $|\Delta_R|$ is reduced but not entirely washed out. Since the simulated effects of the $5D_{3/2}$ level damping largely conform with our experimental observations, we believe that processes consistent with the $5D_{3/2}$ collisional dephasing, such as $5D_{3/2}$ hyperfine-changing collisions and depolarization, are the most prevalent in our experiment.

Finally, based on Fig. 4(e), Rydberg-state dephasing is deemed unimportant because it does not raise the EIT mode 3, it does not significantly attenuate the EIT mode 2 and the pattern of alternating horizontal EIT and EIA stripes at large $|\Delta_R|$, and it enhances the regions of EIA that break up the EIT mode 1 feature instead of eliminating them.

From Fig. 4 we conclude that inert-gas-induced $5D_{3/2}$ hyperfine dephasing should explain most of the differences between the measurements in Figs. 3 and 2. As to EIT

mode 3, we argue that the level broadening of $5D_{3/2}$ caused by the $5D_{3/2}$ hyperfine dephasing leads to a population of near-zero-velocity atoms in $5D_{3/2}$ even at large detunings Δ_D, generated via resonant excitation by the weak EIT probe beam and off-resonant excitation by the more intense EIT dressing beam. Due to their near-zero velocity, these atoms become resonantly excited into the Rydberg state at $\Delta_R \approx 0$, leading to a reduced population in $5P_{1/2}$. The latter, in turn, manifests as the EIT mode 3 band, which occurs at $\Delta_R \approx 0$ and stretches over a wide range of Δ_D.

The above conclusions are reinforced by a simulation result in Fig. 3(d), where we have used our 10-level model and added collisional hyperfine-changing transitions between all $|5D_{3/2}, F'' = *\rangle$ hyperfine states at transition rates of $\Gamma_{mn} = 2\pi \times 1.5$ MHz, with both m and n counting from $F'' = 2$ to $F'' = 4$ and $m \neq n$. We observe good qualitative agreement with the experimental result in Fig. 3(a). The full 10-level simulations also confirm that the effects of hyperfine level dephasing and hyperfine-changing transitions in the EIT spectrum are largely the same. We finally note that the Rb $5D$ hyperfine collision rates assumed in Figs. 3(d) and 4(d) are qualitatively consistent with the results in [48,49], which showed line broadening of up to about 5 MHz per 100 mTorr of Ar.

VIII. DISCUSSION AND CONCLUSION

We have investigated hyperfine effects of the $5D_{3/2}$ level in Rb three-photon EIT on the cascade $5S_{1/2} \to 5P_{1/2} \to 5D_{3/2} \to 25F_{5/2}$ in a Rb vapor cell at 300 K. We found two modes of EIT as well as a pattern of EIT and EIA features that are related to the $5D_{3/2}$ hyperfine structure. Adding a low-pressure Ar gas at 50 mTorr caused significant changes, including the third EIT mode, which we mostly attribute to hyperfine-changing collisions and depolarization of the $5D_{3/2}$ level, the highest excited state of the cascade system that is not a Rydberg state. Our results indicate that EIT and EIA are, globally, of similar significance, both without and with 50 mTorr of Ar gas. The spectroscopic maps in the (Δ_R, Δ_D) plane break up into regions in which either EIT or EIT is prevalent. The experimental observations were reproduced at a good qualitative level by simulations, which were also essential in isolating the causes for the observed inert-gas-induced changes.

The measured and simulated results presented in Figs. 2 and 3 differ in some details. The differences may, in part, be due to environmental magnetic fields that were not shielded in the experiment. Also, the three laser beams may have had polarization errors of up to $\sim 10\%$ due to the use of polarization-maintaining fibers. More fundamentally, we also have neglected optical pumping in our model. Magnetic fields and polarization errors would introduce m_F mixing between all m_F levels and would, in generic cases, lift the degeneracy between manifolds with positive and negative m_F. Without

additional F states, the dimension of the (sub-)spaces subject to Hamiltonian evolution would increase from 10 to 70. At this point, it would become reasonable to also include optical pumping into all F states of the system, which would further increase the state space to 84 (corresponding to $84^2 - 1 = 7055$ independent real elements of the density operator). In addition, the simulation would involve nine or more additional parameters (three magnetic-field components, two Stokes parameters of three polarized fields, etc.). The problem could be addressed using a stochastic method of solving the Lindblad equation based on ensembles of wave-function "trajectories" [40,41]. This effort is beyond the scope of the present paper. Further, in our present work, we have computed steady-state solutions of the density operator. In the case of an added inert gas, the atoms are subject to spatial diffusion dynamics and velocity-changing collisions, which may prolong the EIT/EIA time constants of the vapor during the laser scans [46,47]. In future research, these topics could also be explored.

Finally, we anticipate that our observations may lead to renewed studies on interactions of alkali-metal Rydberg atoms with inert gases, especially studies involving excited electronic states [50]. Previously, line broadening and line shifts in similar systems have attracted considerable attention [48,49,51–53]. Our results point to state-dependent hyperfine collisions, revealed by additional lines in multiphoton Rydberg-EIT spectra. In view of the signal-to-noise ratio seen in our work, we believe that extended studies with Ar, Ne, N_2, and other gases at pressures up to about 100 mTorr would appear promising. Future probes of collisions in Rydberg-EIT would be of interest in the context of recent advanced theoretical studies on alkali-metal-noble-gas collisions [54] as well as developments in modern vapor cell technologies [55]. Further, many-body spin interactions in such systems are of interest in room-temperature quantum information methods [32].

DATA AVAILABILITY

The data that support the findings of this article are not publicly available. The data are available from the authors upon reasonable request.

[1] K.-J. Boller, A. Imamoğlu, and S. E. Harris, Observation of electromagnetically induced transparency, Phys. Rev. Lett. **66**, 2593 (1991).

[2] Q.-Y. Liang, A. V. Venkatramani, S. H. Cantu, T. L. Nicholson, M. J. Gullans, A. V. Gorshkov, J. D. Thompson, C. Chin, M. D. Lukin, and V. Vuletić, Observation of three-photon

bound states in a quantum nonlinear medium, Science **359**, 783 (2018).

[3] D. F. Phillips, A. Fleischhauer, A. Mair, R. L. Walsworth, and M. D. Lukin, Storage of light in atomic vapor, Phys. Rev. Lett. **86**, 783 (2001).

[4] A. K. Mohapatra, T. R. Jackson, and C. S. Adams, Coherent optical detection of highly excited Rydberg states using electromagnetically induced transparency, Phys. Rev. Lett. **98**, 113003 (2007).

[5] J. A. Sedlacek, A. Schwettmann, H. Kübler, R. Löw, T. Pfau, and J. P. Shaffer, Microwave electrometry with Rydberg atoms in a vapour cell using bright atomic resonances, Nat. Phys. **8**, 819 (2012).

[6] C. L. Holloway, J. A. Gordon, S. Jefferts, A. Schwarzkopf, D. A. Anderson, S. A. Miller, N. Thaicharoen, and G. Raithel, Broadband Rydberg atom-based electric-field probe for SI-traceable, self-calibrated measurements, IEEE Trans. Antennas Propag. **62**, 6169 (2014).

[7] C. Carr, M. Tanasittikosol, A. Sargsyan, D. Sarkisyan, C. S. Adams, and K. J. Weatherill, Three-photon electromagnetically induced transparency using Rydberg states, Opt. Lett. **37**, 3858 (2012).

[8] N. Thaicharoen, K. R. Moore, D. A. Anderson, R. C. Powel, E. Peterson, and G. Raithel, Electromagnetically induced transparency, absorption, and microwave-field sensing in a Rb vapor cell with a three-color all-infrared laser system, Phys. Rev. A **100**, 063427 (2019).

[9] P. Thoumany, Th. Germann, T. Hänsch, G. Stania, L. Urbonas, and Th. Becker, Spectroscopy of rubidium Rydberg states with three diode lasers, J. Mod. Opt. **56**, 2055 (2009).

[10] D. P. Fahey and M. W. Noel, Excitation of Rydberg states in rubidium with near infrared diode lasers, Opt. Express **19**, 17002 (2011).

[11] L. A. M. Johnson, H. O. Majeed, and B. T. H. Varcoe, A three-step laser stabilization scheme for excitation to Rydberg levels in ⁸⁵Rb, Appl. Phys. B **106**, 257 (2012).

[12] S. M. Bohaichuk, F. Ripka, V. Venu, F. Christaller, C. Liu, M. Schmidt, H. Kübler, and J. P. Shaffer, Three-photon Rydberg-atom-based radio-frequency sensing scheme with narrow linewidth, Phys. Rev. Appl. **20**, L061004 (2023).

[13] A. Duspayev, R. Cardman, D. A. Anderson, and G. Raithel, High-angular-momentum Rydberg states in a room-temperature vapor cell for dc electric-field sensing, Phys. Rev. Res. **6**, 023138 (2024).

[14] N. Prajapati, J. W. Kunzler, A. B. Artusio-Glimpse, A. Rotunno, S. Berweger, M. T. Simons, C. L. Holloway, C. M. Gardner, M. S. Mcbeth, and R. A. Younts, High angular momentum coupling for enhanced Rydberg-atom sensing in the very-high frequency band, J. Appl. Phys. **135**, 074402 (2024).

[15] G. Allinson, M. J. Jamieson, A. R. Mackellar, L. Downes, C. S. Adams, and K. J. Weatherill, Simultaneous multi-band radio-frequency detection using high-orbital-angular-momentum states in a Rydberg-atom receiver, Phys. Rev. Res. **6**, 023317 (2024).

[16] L. Ma, E. Paradis, and G. Raithel, DC electric fields in electrode-free glass vapor cell by photoillumination, Opt. Express **28**, 3676 (2020).

[17] R. C. Brown, B. Kayim, M. A. Viray, A. R. Perry, B. C. Sawyer, and R. Wyllie, Very-high- and ultrahigh-frequency electric-field detection using high angular momentum Rydberg states, Phys. Rev. A **107**, 052605 (2023).

[18] P. K. Elgee, J. C. Hill, K.-J. E. LeBlanc, G. D. Ko, P. D. Kunz, D. H. Meyer, and K. C. Cox, Satellite radio detection via dual-microwave Rydberg spectroscopy, Appl. Phys. Lett. **123**, 084001 (2023).

[19] D. A. Anderson, G. Raithel, M. Simons, and C. L. Holloway, Quantum-optical spectroscopy for plasma electric field measurements and diagnostics, arXiv:1712.08717.

[20] S. Alexiou, A. Weingarten, Y. Maron, M. Sarfaty, and Ya. E. Krasik, Novel spectroscopic method for analysis of nonthermal electric fields in plasmas, Phys. Rev. Lett. **75**, 3126 (1995).

[21] H. Park, R. Ali, and T. F. Gallagher, Probing the fields in an ultracold plasma by microwave spectroscopy, Phys. Rev. A **82**, 023421 (2010).

[22] B. M. Goldberg, T. Hoder, and R. Brandenburg, Electric field determination in transient plasmas: *in situ* & non-invasive methods, Plasma Sources Sci. Tech. **31**, 073001 (2022).

[23] A. Duspayev and G. Raithel, Electric field analysis in a cold-ion source using Stark spectroscopy of Rydberg atoms, Phys. Rev. Appl. **19**, 044051 (2023).

[24] N. Bassim, K. Scott, and L. A. Giannuzzi, Recent advances in focused ion beam technology and applications, MRS Bull. **39**, 317 (2014).

[25] J. Gierak, P. Mazarov, L. Bruchhaus, R. Jede, and L. Bischoff, Review of electrohydrodynamical ion sources and their applications to focused ion beam technology, J. Vac. Sci. Technol. B **36**, 06J101 (2018).

[26] B. Knuffman, A. V. Steele, and J. J. McClelland, Cold atomic beam ion source for focused ion beam applications, J. Appl. Phys. **114**, 044303 (2013).

[27] A. J. McCulloch, B. M. Sparkes, and R. E. Scholten, Cold electron sources using laser-cooled atoms, J. Phys. B **49**, 164004 (2016).

[28] B. Yang, J. Gao, T. Zhang, and J. Wang, Electromagnetically induced transparency without a Doppler background in a multilevel ladder-type cesium atomic system, Phys. Rev. A **83**, 013818 (2011).

[29] J. M. Kondo, N. Šibalić, A. Guttridge, C. G. Wade, N. R. De Melo, C. S. Adams, and K. J. Weatherill, Observation of interference effects via four-photon excitation of highly excited Rydberg states in thermal cesium vapor, Opt. Lett. **40**, 5570 (2015).

[30] A. Duspayev and G. Raithel, Spectroscopy of the ⁸⁵Rb $4D_{3/2}$ state for hyperfine-structure determination, New J. Phys. **25**, 093015 (2023).

[31] S. D. Badger, I. G. Hughes, and C. S. Adams, Hyperfine effects in electromagnetically induced transparency, J. Phys. B **34**, L749 (2001).

[32] O. Katz, R. Shaham, and O. Firstenberg, Quantum interface for noble-gas spins based on spin-exchange collisions, PRX Quantum **3**, 010305 (2022).

[33] F. Nez, F. Biraben, R. Felder, and Y. Millerioux, Optical frequency determination of the hyperfine components of the $5S_{1/2}$-$5D_{3/2}$ two-photon transitions in rubidium, Opt. Commun. **102**, 432 (1993).

[34] D. Manzano, A short introduction to the Lindblad master equation, AIP Adv. **10**, 025106 (2020).

[35] D. A. Steck, Rubidium 85 D line data, available at https://steck.us/alkalidata/ (2024).

[36] F. Le Kien, P. Schneeweiss, and A. Rauschenbeutel, Dynamical polarizability of atoms in arbitrary light fields: General theory and application to cesium, Eur. Phys. J. D **67**, 92 (2013).

[37] M. S. Safronova, C. J. Williams, and C. W. Clark, Relativistic many-body calculations of electric-dipole matrix elements, lifetimes, and polarizabilities in rubidium, Phys. Rev. A **69**, 022509 (2004).

[38] M. S. Safronova and U. I. Safronova, Critically evaluated theoretical energies, lifetimes, hyperfine constants, and multipole polarizabilities in ^{87}Rb, Phys. Rev. A **83**, 052508 (2011).

[39] D. Sheng, A. Pérez Galván, and L. A. Orozco, Lifetime measurements of the $5d$ states of rubidium, Phys. Rev. A **78**, 062506 (2008).

[40] Y. Xue, L. Hao, Y. Jiao, X. Han, S. Bai, J. Zhao, and G. Raithel, Rydberg electromagnetically induced transparency in a large Hilbert space, Phys. Rev. A **99**, 053426 (2019).

[41] L. Zhang, S. Bao, H. Zhang, G. Raithel, J. Zhao, L. Xiao, and S. Jia, Interplay between optical pumping and Rydberg EIT in magnetic fields, Opt. Express **26**, 29931 (2018).

[42] H. S. Moon, L. Lee, and J. B. Kim, Double resonance optical pumping effects in electromagnetically induced transparency, Opt. Express **16**, 12163 (2008).

[43] Z.-S. He, J.-H. Tsai, Y.-Y. Chang, C.-C. Liao, and C.-C. Tsai, Ladder-type electromagnetically induced transparency with optical pumping effect, Phys. Rev. A **87**, 033402 (2013).

[44] H.-J. Su, J.-Y. Liou, I-C. Lin, and Y.-H. Chen, Optical pumping effects on high-contrast Rydberg electromagnetically induced transparency, J. Appl. Phys. **132**, 244401 (2022).

[45] N. Thaicharoen, R. Cardman, and G. Raithel, Rydberg electromagnetically induced transparency of ^{85}Rb vapor in a cell with Ne buffer gas, Phys. Rev. Appl. **21**, 064004 (2024).

[46] B. Dash, N. Thaicharoen, E. Paradis, A. Duspayev, and G. Raithel, Rydberg electromagnetically induced transparency of ^{85}Rb vapor in Ar, Ne, and N_2 gases, APL Quantum **2**, 016132 (2025).

[47] M. Lei, S. P. Eckel, E. B. Norrgard, N. Prajapati, A. B. Artusio-Glimpse, M. T. Simons, and C. L. Holloway, Collisional broadening of ^{85}Rb Rydberg levels: Conclusions for vapor-cell manufacture, Phys. Rev. Appl. **23**, 034028 (2025).

[48] A. Sargsyan, D. Sarkisyan, U. Krohn, J. Keaveney, and C. Adams, Effect of buffer gas on an electromagnetically induced transparency in a ladder system using thermal rubidium vapor, Phys. Rev. A **82**, 045806 (2010).

[49] N. D. Zameroski, G. D. Hager, C. J. Erickson, and J. H. Burke, Pressure broadening and frequency shift of the $5S_{1/2} \rightarrow 5D_{5/2}$ and $5S_{1/2} \rightarrow 7S_{1/2}$ two photon transitions in ^{85}Rb by the noble gases and N_2, J. Phys. B **47**, 225205 (2014).

[50] I. Dubourg, M. Ferray, J. P. Visticot, and B. Sayer, Experimental investigation of the Rb (6S or 4D)-rare gas interaction: Determination of interaction potentials and oscillator strengths, J. Phys. B: Atom. Mol. Phys. **19**, 1165 (1986).

[51] W.-Ü L. Brillet and A. Gallagher, Inert-gas collisional broadening and shifts of Rb Rydberg states, Phys. Rev. A **22**, 1012 (1980).

[52] D. C. Thompson, E. Kammermayer, B. P. Stoicheff, and E. Weinberger, Pressure shifts and broadenings of Rb Rydberg states by Ne, Kr, and H_2, Phys. Rev. A **36**, 2134 (1987).

[53] M. E. Henry and R. M. Herman, Collisional broadening of Rydberg atom transitions by rare gas perturbers, J. Phys. B **35**, 373 (2002).

[54] A. A. Medvedev, V. V. Meshkov, A. V. Stolyarov, and M. C. Heaven, *Ab initio* interatomic potentials and transport properties of alkali metal (M = Rb and Cs)–rare gas (Rg = He, Ne, Ar, Kr, and Xe) media, Phys. Chem. Chem. Phys. **20**, 25974 (2018).

[55] J. Kitching, S. Knappe, and E. A. Donley, Atomic sensors—A review, IEEE Sens. J. **11**, 1749 (2011).